



Antenna Structures for Optical Coupling in Quantum-Well Infrared Detectors

by William A. Beck, Mark S. Mirotznik, and Thomas S. Faska

ARL-TR-1533

March 1998

The findings in this report are not to be construed as an official Department of the Army position unless so designated by other authorized documents.

Citation of manufacturer's or trade names does not constitute an official endorsement or approval of the use thereof.

Destroy this report when it is no longer needed. Do not return it to the originator.

Army Research Laboratory

Adelphi, MD 20783-1197

ARL-TR-1533

March 1998

Antenna Structures for Optical Coupling in Quantum-Well Infrared Detectors

William A. Beck

Sensors and Electron Devices Directorate, ARL

Mark S. Mirotznik

The Catholic University of America

Washington, DC

Thomas S. Faska

Sanders, a Lockheed Martin Company

Nashua, NH

Abstract

Predicted performance for antenna-coupled, quantum-well infrared photodetectors (QWIPs) is presented. These structures contain a patterned metal antenna layer and dielectric backplane reflector in place of the usual metal phase grating. When illuminated by normally incident plane-wave illumination, the antenna structures generate both evanescent and propagating modes that have the required polarization to be absorbed by the QW stack. An undersampled spectral technique is also demonstrated for using the finite-difference, time-domain (FDTD) technique to compute spectral quantum efficiency in a single FDTD run.

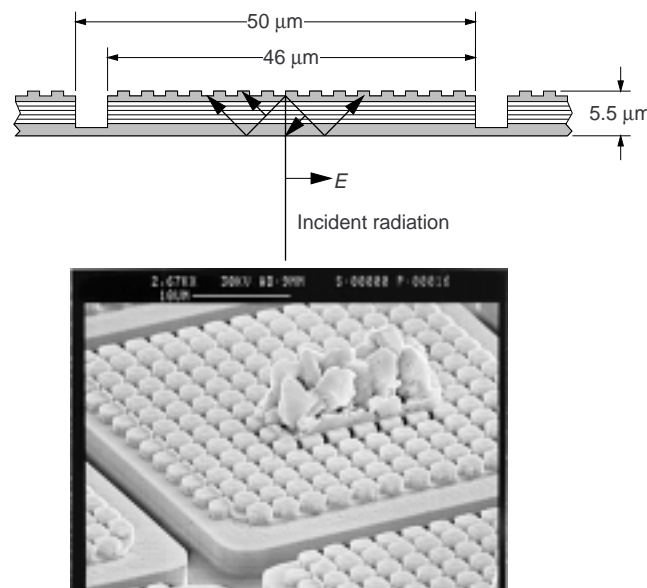
Introduction

Quantum-well infrared photodetectors (QWIPs) provide many attractive features for use in large focal plane arrays (FPAs). Most QWIPs are grown on GaAs substrates, for which large wafers (up to 6 in. diameter) are available. Reproducible and precise growth using established III-V molecular beam epitaxy (MBE) and a simple fabrication process has produced high yields in both detectors and FPAs. The large wafers and uniformity that can be achieved with MBE offer a unique capability for low-cost production of large, high-sensitivity staring FPAs. 640×480 FPAs with thermal sensitivity around 20 mK are now typical.

However, the quantum efficiency (QE) of QWIP detectors is typically lower than that of direct bandgap detectors, such as HgCdTe photodiodes. A typical QWIP QE is in the range of 10 to 30 percent, while direct bandgap detectors achieve 70 to 80 percent. The spectral bandwidth of QWIPs is also typically limited to $\sim 1.5 \mu\text{m}$, further reducing the detection efficiency for blackbody targets. For many applications in which the detection sensitivity is limited by the charge well capacity of the readout circuitry, the difference in QE has no effect. However, in other applications—e.g., systems operating at high frame rates or in low backgrounds—higher QE and bandwidth would be beneficial.

A typical QWIP pixel is shown in figure 1. It consists of a QW stack surrounded by two contact layers and an optical coupling structure (OCS), such as a metalized diffraction grating. The OCS is required to scatter or diffract normally incident light into modes with a component of electric field perpendicular to the QWs. The efficiency of this scattering or diffraction process, and the degree to which the scattered light is trapped inside the pixel to make multiple passes through the QW stack, are major factors that determine the QE of the QWIP.

Figure 1. Typical grating-coupled QWIP pixel.



Previous QWIPs have used a variety of metalized diffraction gratings, including periodic [1–5] and pseudorandom [6] etched gratings, as well as periodic planar gratings [7]. These structures are generally designed to couple via propagating modes above the grating. With periodic gratings, the period is chosen so that the grating is near resonance, i.e., so that normally incident light is diffracted at an angle slightly less than 90° from the normal. In a large pixel, the diffracted light makes a pass through the QW stack, is totally internally reflected by the GaAs/air boundary, makes a second pass through the QW stack, and is then coherently rediffracted back out of the sample when it reimpinges on the grating [6]. This coherent rediffraction happens when all of the diffracted orders have the same path length between leaving and returning to the grating, so that they return with the same phase relationship with which they left. The pseudorandom grating scatters normally incident light into a wider range of angles so that the totally internally reflected modes reimpinge on the grating with randomized phase, thereby avoiding coherent rediffraction out of the QWIP, and permitting additional passes through the QW stack. In large pixels, a significant improvement of QE was observed with the pseudorandom over the periodic grating. However, the improvement decreases in smaller pixels [8]. The reduction in QE for smaller pixels tends to be a characteristic of all QWIPs that rely on propagating modes, and is a problem for the small (typically $\sim 24\text{ }\mu\text{m}$) pixels used in large arrays. Periodic gratings also couple effectively in a relatively narrow ($1\text{--}2\text{ }\mu\text{m}$) spectral band. Pseudorandom gratings typically have a wider spectral band corresponding to the wider range of spatial frequencies in their patterns.

Several groups have demonstrated designs in which the “grating” is etched through the QW stack, either in a two-dimensional square lattice (the “enhanced,” or EQWIP) [9] or as a set of parallel V-shaped grooves (the “corrugated,” or C-QWIP) [10]. These designs depend less on propagating modes and more on localized modes, so their performance is degraded much less in small pixels. The V-groove structure [10] also has a relatively wide spectral bandwidth.

In this report, we investigate the expected performance of antenna-coupled QWIPs. These structures employ an array of planar metal antennas in close proximity to the QW stack, so that the near-field modes of the antennas couple to the QWs.

Design and modeling of optical coupling in QWIPs is difficult because the absorption takes place in the near-field of the grating (invalidating the common Fresnel and Fraunhofer approximations), the features are comparable to the wavelength of the optical radiation, and the anisotropic absorption of the QW stack requires use of a vector propagation model (except in certain simple geometries). For structures in which the electromagnetic modes in the grating are known, such as the linear lamellar grating or the two-dimensional array of box cavities, the coupling can be calculated by the modal expansion method (MEM) [4]. However, the modes are known for only a few simple structures and, even then, only

for the case of perfect electric conductor (PEC) grating metal. For example, while it is possible to model a two-dimensional array of square cavities, the complementary structure with square pedestals is much harder.

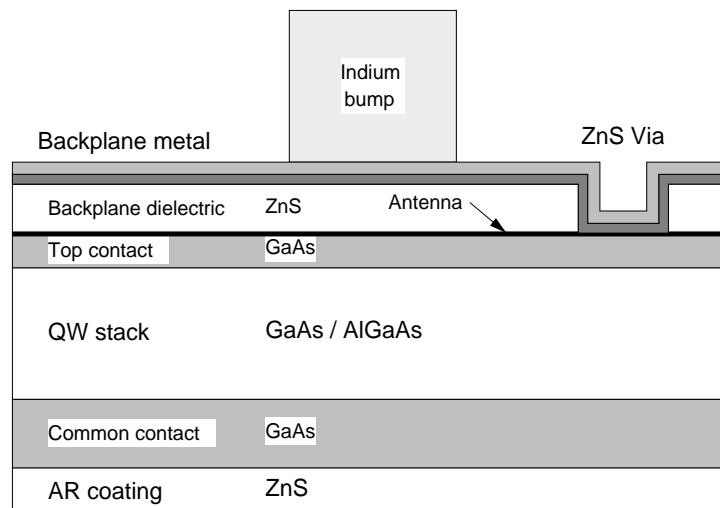
Previous experimental results and the results presented later in this report show that finite conductivity of the metal used for the grating or antenna can significantly degrade QE. For example, earlier experiments [4] indicated that detectors with AuGe contacts had a QE that was 70 percent of the QE for detectors with pure gold contacts. The results in this report suggest that the finite conductivity of even pure gold is significant.

This report describes the use of the finite-difference, time-domain (FDTD) method, as well as a modified MEM for calculating optical QE in QWIPs. An undersampled spectral FDTD technique was used that is especially advantageous for QWIP modeling because it permits calculation of a full spectrum of QE versus wavelength in a single FDTD run. The three-dimensional absorption pattern can also be visualized at any of the wavelengths in the spectrum. The modified MEM is used to model QE in infinitely periodic, antenna-coupled QWIPs.

Antenna-Coupled QWIP Structure

The basic elements of an antenna-coupled QWIP are shown in figure 2. In addition to the standard QW stack with common and top contact layers and antireflection coating, the structure contains a planar metal antenna layer, backplane dielectric, and backplane metal. In antenna terminology, the backplane dielectric and metal serve to reflect the back radiation modes of the antenna to the front. Alternatively, they can be thought to reflect light that passes through the antenna back into the absorbing part of the detector. The backplane structure permits the antenna to be used in a “reflection” configuration rather than the arrangement used previously for transmission planar gratings [7].

Figure 2. Cross section of antenna-coupled pixel.



The antenna dimensions are largely determined by the wavelength band(s) that are to be detected. For example, the spiral antenna (to be described later) fits in a square that is about $6\text{ }\mu\text{m}$ on a side. To provide coupling for the whole pixel, the antenna pattern is replicated in a periodic array that nearly fills the pixel. The resulting periodic antenna pattern can couple through both propagating Floquet modes generated by the periodic array and bound antenna modes. If the propagating modes make a dominant contribution to QW absorption, then the structure is similar in operation to the planar metal grating. However, when the QW coupling arises mainly through bound antenna modes, a potentially broadband coupling is achieved that is scalable to small pixels.

Use of planar metal layers eliminates the need for a grating etch and the potential nonuniformity associated with that etch. On the other hand, the antenna structure requires deposition of the backplane dielectric and often involves definition of fine features in the antenna. All the processing, except for deposition of the antireflection (AR) coating, is done on the front (MBE growth) side of the wafer, so there is no need for backside processing of individual die or handling of fully thinned wafers, as with some other approaches.

Modeling Techniques

Two models were used to calculate the absorption QE of QWIP pixels. The first method is an MEM, modified to include an arbitrarily patterned, finite or perfectly conducting antenna layer. The procedure assumes the antenna pattern is periodic and infinite in lateral extent.

The second model is based on the three-dimensional FDTD method. It can model arbitrarily shaped, grating- or antenna-coupled, finite-sized QWIP pixels. Finite-conductivity metals can be used, although with some limitations.

Coupled Mode (Infinite Pixel)

The variation of the MEM that was used for infinitely periodic, antenna-coupled QWIPs was implemented using the 4×4 matrix method described by Yeh [11]. This transfer-matrix method rigorously computes vector electromagnetic propagation of a plane wave through a stack of uniaxially anisotropic planar layers. In the case of a QWIP pixel containing a periodic array of antennas, the 4×4 matrix method was applied to each of the Floquet modes independently, except at the antenna layer, where the Floquet modes were mixed to achieve the required boundary conditions along the antenna surface. The antenna layer was assumed to be a patterned sheet conductor with zero thickness and a specified (sometimes infinite) sheet conductance. The calculation enforced the condition

that the tangential electric fields were zero along the metal parts of the antenna (for a perfectly conducting antenna metal) or that sheet current (and therefore the discontinuity in tangential magnetic field across the antenna layer) was proportional to the tangential electric field through Ohm's law:

$$\vec{J}_{\text{metal}} = \sigma_{\text{metal}} \vec{E}_{\parallel} . \quad (1)$$

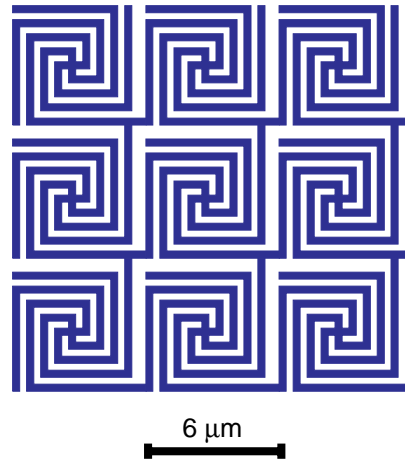
The antenna was laid out on a square grid. For example, a unit cell of the spiral antenna (see fig. 3) was laid out on a 19×19 mesh. The 19×19 real-space mesh was then used in a solution with a set of 19×19 Floquet modes.

Finite-Difference Time Domain (Finite Pixel)

A QWIP pixel is a somewhat challenging structure in which to compute electromagnetic coupling. The structure is inhomogeneous, including multiple layers of dielectrics and finite-conductivity metals. The QW stack itself is anisotropic. Finally, the structure has many potential resonances that result from the periodicity of the grating, as well as from the pixel cavity itself.

The FDTD method [12,13] is well suited to solving problems of this type. The method is a direct solution for Maxwell's time-dependent curl equations based on volumetric sampling of the unknown field distribution within and near the pixel over a period of time. The sampling in space is typically at 10 to 20 samples per wavelength (in the material). The sampling in time is selected to ensure numerical stability. For the results presented here, the QWIP pixel structures were first designed and gridded using a custom Mathematica notebook. The FDTD calculations were then run using a commercial FDTD program called XFDTD [14]. Finally, the results were analyzed using custom software in C++.

Figure 3. 3×3 array of four-arm spiral antennas. Metal is dark.



High, but finite-conductivity metals present a problem in FDTD (and other numerical electromagnetic techniques). This is because the fields change so rapidly near the surface of such a metal, thereby requiring an unreasonably small grid spacing to accurately describe the fields. For example, a grid spacing of $0.3\ \mu\text{m}$ is acceptable in most sections of a QWIP being illuminated with incident radiation at $9.0\ \mu\text{m}$ wavelength, since $0.3\ \mu\text{m}$ is about $1/10$ the wavelength in GaAs. However, a high-conductivity metal such as gold may have a skin depth of $\sim 100\ \text{\AA}$, requiring a grid spacing of $\sim 10\ \text{\AA}$, which requires far too many grid cells to calculate in any reasonable time. Instead of this “brute-force” approach, we used the “synthetic conductivity” method [15], which employs a derived conductivity value that, when used in the FDTD difference equations, yields the correct surface impedance. Therefore, the fields outside the metal are nearly correct, even though the fields inside may not be. It should be noted that although the synthetic conductivity method has been shown to yield the correct reflectance for planar surfaces [15], its accuracy on highly structured surfaces such as gratings has not been proven yet. Also, accuracy may be worse for thin conductors such as the antenna that are less than five cells thick.

The appropriate synthetic FDTD conductivity is related to the true conductivity through [15]

$$\sigma_{\text{FDTD}} = \frac{1}{\Delta z} \sqrt{\frac{\sigma_{\text{True}}}{\omega \mu}} , \quad (2)$$

where Δz is the cell size, ω is the angular frequency of the illumination, and μ is the magnetic permeability. For a good conductor, we use the approximation that the reflectivity is approximately related to the conductivity through [16]

$$1 - R \cong 2 \sqrt{\frac{2\varepsilon_0 \omega}{\sigma_{\text{True}}}} , \quad (3)$$

where ε_0 is the permittivity of free space. Eliminating σ_{True} from the equations and assuming nonmagnetic materials yields the frequency-independent relationship,

$$\sigma_{\text{FDTD}} = \frac{1}{\Delta z} \sqrt{\frac{2\varepsilon_0}{\mu_0} \left(\frac{2}{1 - R} \right)} \cong \frac{3.75 \times 10^{-3} \text{S}}{\Delta z} \left(\frac{2}{1 - R} \right) . \quad (4)$$

The reflectance and conductivity of pure gold depend on the morphology of the deposited film. Use of a published bulk conductivity [17] of $2.44\ \mu\Omega\text{-cm}$ in equation (3), at a frequency corresponding to a wavelength of $10.0\ \mu\text{m}$, yields a reflectivity of 98.11 percent and a synthetic conductivity of $1.32 \times 10^6\ \text{S/m}$ for $\Delta z = 0.3\ \mu\text{m}$. On the other hand, published optical properties [11] yield a reflectance of 99.02 percent and real and synthetic conductivities of $1.40 \times 10^8\ \text{S/m}$ and $2.56 \times 10^6\ \text{S/m}$, respectively. Because these represent pure gold, they are an upper limit to the conductivity and reflectance that can be achieved in a real QWIP. The actual conductivity might be significantly lower, especially if alloyed contacts are used.

Other material properties used, shown in table 1, were based on published values as well as fits to experimental data. The QW stack is composed of many alternating layers of, for example, GaAs and AlGaAs; however, since the layer thicknesses are much less than a wavelength, the stack was modeled as a homogeneous material with spatially averaged properties. The permittivity of the QW stack was deduced from published data for GaAs and AlAs and from the peak wavelength of earlier grating-coupled QWIPs. The conductivity perpendicular to the QW stack was deduced from Brewster-angle absorption measurements on unprocessed MBE wafers. Although the frequency-dependent conductivity of the QW stack can be incorporated into the FDTD calculations, we used a constant conductivity for all results presented here so that the coupling efficiency could be seen over a broad spectral range.

Two types of FDTD runs were used. The most straightforward were the steady-state runs, in which the incident field on the pixel was a sinusoid at a single frequency. In this case the FDTD program was allowed to run until the fields reached a steady state. The XFDTD program was set up to output the absorption at each point in the QW stack so that the total absorption, and hence the QE, could be computed. Although simple, this technique yields the QE at only a single wavelength.

In the second technique, the incident field on the pixel was a Gaussian-modulated sinusoid, as shown in figure 4a. The Gaussian modulation in the time domain corresponds to a Gaussian envelope of incident frequencies in the frequency domain. Since the FDTD method (and all of our materials) are linear, the different frequencies in the incident field propagate independently through the time stepping. Therefore, as shown in figure 4, Fourier analysis on the time-dependent absorption at each point in the QW stack yields the absorption and QE at all of the incident frequencies. In other words, we get a full spectrum of QE in roughly the same time that the steady-state method yields the value at a single wavelength.

Table 1. Material properties used in FDTD calculations.

Material	Parallel to QWs		Perpendicular to QWs	
	Permittivity (Siemens/m)	Conductivity	Permittivity (Siemens/m)	Conductivity
GaAs contact	9.92	0.0	9.92	0.0
QW stack	9.92	0.0	9.92	462
Gold	1.0	1.0×10^6 (*)	1.0	1.0×10^6 (*)
ZnS	5.52	0.0	5.52	0.0
Epoxy	2.25	0.0	2.25	0.0

(*) "Synthetic" conductivity (see text).

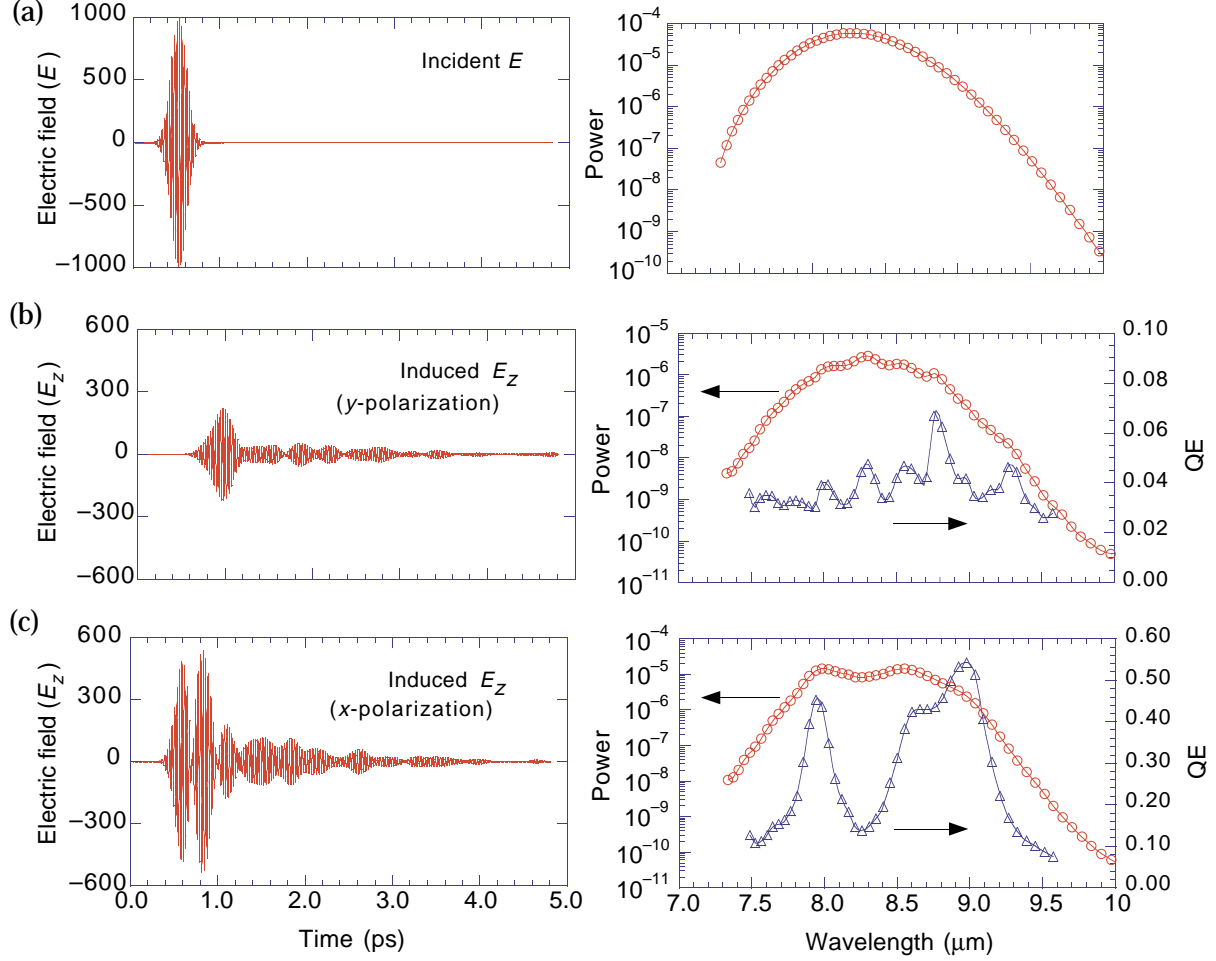


Figure 4. Time-dependent electric fields (left column) and incident and absorbed power and QE (right column) near center of 50- μm pixel with 3- μm period linear grating along y-direction: (a) incident field (Gaussian-modulated 35.3-THz sinusoid), (b) induced E_z for y-polarized incident field, and (c) induced E_z for x-polarized incident field.

The main problems with the Gaussian-modulated approach are practical ones. Saving the full set of time-dependent fields at all grid points in the QW stack generates huge amounts of data. For example, using the XFDTD “field snapshot” files to output the fields at all time steps generates over 22 GB of data. Writing the output files also slows the program considerably. However, it is not necessary to save data at all time steps. First, the time step that is required for stability in the FDTD method is highly oversampled relative to that required by the Nyquist criterion. For example, the Courant timestep required for stability at frequency f in a material with index n and with cell size equal to 1/10 the wavelength is

$$\Delta t = \frac{1}{10 f n \sqrt{3}} , \quad (5)$$

which is $5n/\sqrt{3}$ times smaller than the Nyquist sampling interval of $1/(2f)$ for that frequency. By sampling the fields at the Nyquist frequency, we reduce the amount of data by a factor of ~ 27 for GaAs with $n = 3.15$. Second, the Gaussian modulation is usually set up with a relatively narrow band of frequencies in the incident field (corresponding, for example, to a wavelength range of $7\text{--}10\text{ }\mu\text{m}$). The narrow bandwidth can be exploited by further undersampling (below the Nyquist frequency) such that the frequency band is aliased down to lower frequencies. If the undersampling ratio is chosen correctly, the shape and amplitude of the original spectrum can be preserved after the aliasing. By combining both techniques, we can undersample by a factor as high as ~ 130 to 140 and still recover the QE at all of the frequencies in the incident field.

Results

Two-Dimensional, Square-Cavity Grating

To facilitate comparison with earlier modeling and with experimental results, we computed the spectral QE for a conventional QWIP with a $3\text{-}\mu\text{m}$ -period square grating using the FDTD method. As shown in figure 5, the structure was an isolated $39\text{-}\mu\text{m}$ pixel with 40 QWs surrounded by $9\text{ }\mu\text{m}$ of “epoxy.” The grating used $2.1\text{-}\mu\text{m}$ square cavities that were $0.6\text{ }\mu\text{m}$ deep. A cell size of $0.3 \times 0.3 \times 0.3\text{ }\mu\text{m}$ was used with 8064 time steps. The time step length was equal to the Courant value of $5.78 \times 10^{-16}\text{ s}$. The electric fields had decayed to less than 1 percent of their peak values by the end of the time stepping.

Figure 6 shows the resultant QE of the structure for different values of the grating metal FDTD conductivity. Several features are noteworthy. First, the high-conductivity ($s = 1 \times 10^7\text{ S/m}$) curve is close to the curve for PEC grating metal, verifying that the synthetic conductivity method gives the appropriate behavior at the high-conductivity limit.

Second, the portion of the high- and perfect-conductor curves above $8\text{ }\mu\text{m}$ are very similar to the curves shown in figure 7 of Andersson and Lundqvist [4], based on the MEM with PEC grating metal. The similarity includes the double-humped main peak between 9 and $10\text{ }\mu\text{m}$, as well as the smaller peak between 8.5 and $9.0\text{ }\mu\text{m}$. This similarity exists even though the layer thicknesses and cavity sizes were not identical.

Figure 5. Cross section of square-grating-coupled structure. Grating is $3\text{-}\mu\text{m}$ period with $2.1 \times 0.6\text{ }\mu\text{m}$ cavities.

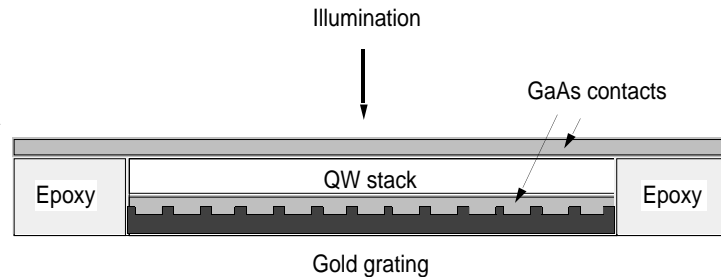


Figure 6. Calculated spectral QE for 39- μm pixel with 3- μm -period, two-dimensional, square-cavity grating. “Synthetic” conductivity corresponding to indicated reflectances is shown. QW absorption strength is constant.

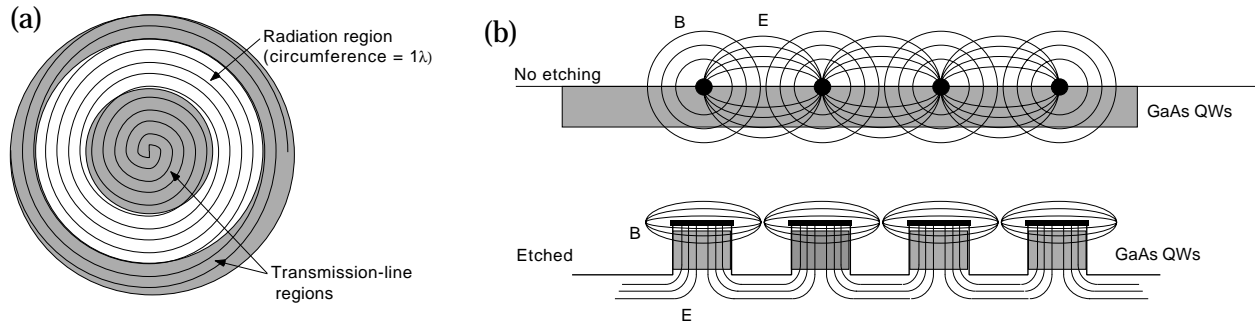
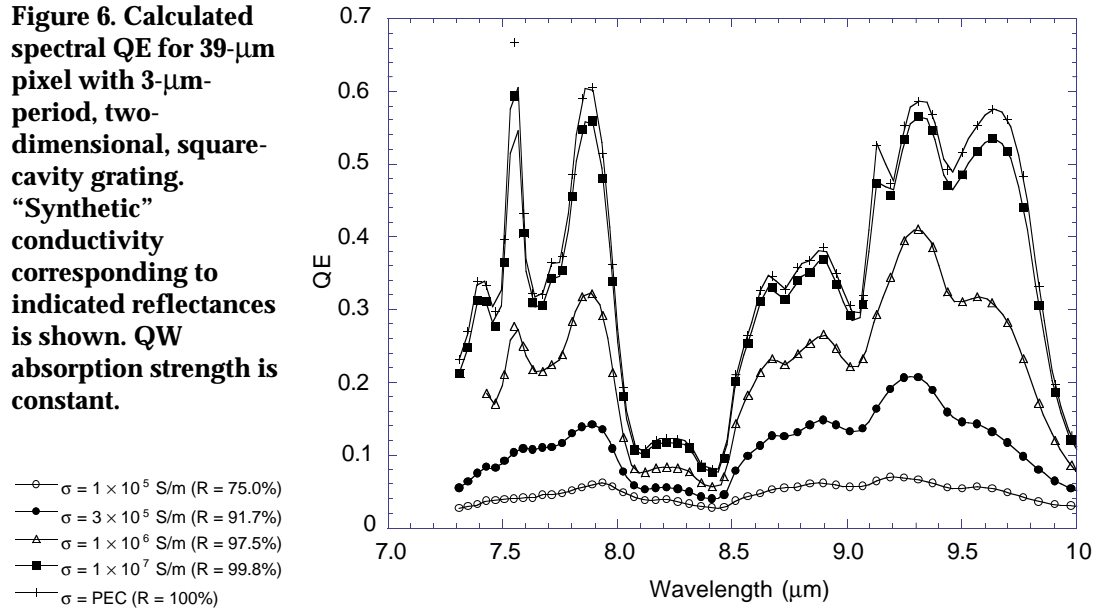


Figure 7. Operation of spiral antenna: (a) operating regions and (b) field distributions in transmission line region with and without etching.

Third, the QE is significantly degraded by finite conductivity, even for conductivities corresponding to $R = 97.5$ percent. Note particularly the suppression of the long-wavelength peak at about $9.65 \mu\text{m}$. This peak is beyond the $9.45\text{-}\mu\text{m}$ resonance of the grating and therefore corresponds to evanescent modes. The evanescent modes (and near-resonance propagating modes) that couple to the QW stack have electric field perpendicular to the grating surface and magnetic field along the surface. The tangential magnetic fields imply surface currents in the grating metal that are suppressed, along with the evanescent modes themselves, when the grating conductivity is reduced. We note that the curve for $R = 91.7$ percent approximately matches the shape and magnitude of many real QWIP detectors, suggesting that grating metal conductivity may be a major factor that limits the performance of these type of QWIPs.

Spiral Antenna

The spiral antenna offers a number of attractive features for use as an optical coupler in QWIPs. It is well known for wide spectral bandwidth, typically 8:1 or even 32:1 in the microwave region [18]. This is much wider than the 2:1 or 3:1 ratio required for multicolor QWIPs. (However, use of a backplane reflector reduces the bandwidth.) Finally, the field patterns around a two- or four-arm spiral antenna have large components perpendicular to the antenna plane, which should strongly couple to a closely placed QW stack.

Figure 7a shows the basic operating regions of a standard spiral antenna. In the so-called radiation zones, the currents in adjacent windings are in phase and lead to radiation of power from the antenna (or absorption of power from an incident field). In the transmission-line regions, the current in adjacent windings is approximately 180° out of phase so that power is carried along the windings as in a standard two-wire transmission line. As indicated in figure 7b, the electric fields in the transmission-line regions have large components perpendicular to the plane of the antenna that can couple to a closely spaced QW stack. The QW stack can be thought of as loading the antenna so that the reradiated power is less than the incident power. This power “loss” from an antenna perspective is the desired detection from a QWIP perspective.

The coupling strength between the antenna modes and the QW stack can be further increased if the QW material between the windings is removed and replaced with a material with a lower refractive index (such as vacuum or ZnS). As shown in figure 7b, the electric field lines tend to flow through the higher index QW material, thereby extending the coupling farther into the QW stack. This removal of about half of the QW material also lowers the dark current by the same ratio.

Figure 3 shows the antenna pattern that was used for this work. The unit cell is a single, four-arm spiral that is replicated in a two-dimensional array to fill the pixel. The individual spirals are interconnected so that a single via hole through the backplane dielectric can be used to make contact to the entire array of antennas, which also acts as one of the electrical contacts to the detector. The square spiral was used to ease fabrication using electron-beam lithography (EBL). The lines and spaces are about $0.32\text{ }\mu\text{m}$ wide, which is easily achievable with EBL. A cell size of $0.16 \times 0.16\text{ }\mu\text{m}$ was used with 19,328 time steps. The time step length was equal to 0.75 times the Courant value, or $2.41 \times 10^{-16}\text{ s}$. The electric fields had decayed to less than 1 percent of their peak values by the end of the time stepping. We modeled a 3×3 array of spirals that includes the interactions between neighboring spirals and would be appropriate for a $20\text{-}\mu\text{m}$ pixel.

Figure 8 shows the calculated spectral QE from the 3×3 array for structures with QW stack thicknesses of 0.33 and 0.83 μm , corresponding to 5 and 12 QWs, respectively. The QEs of 20 to 30 percent for 12 QWs and 10 to 20 percent for 5 QWs are relatively high, considering the small numbers of QWs. Furthermore, since the dark-current-limited D^* is proportional to $\text{QE} (N_W I_d)^{-1/2}$, where N_W is the number of wells and I_d is the dark current, a QE of 20 percent with 12 QWs (or 13 percent with 5 QWs) and a 50-percent dark current reduction will yield the same D^* as 52 percent QE with 40 QWs and full dark current. The figure also shows curves for a synthetic conductivity of 10^6 S/m . The QE is substantially reduced below the PEC curves, but as previously stated, the physical conductivity implied by this synthetic conductivity is not clear for a layer only one cell thick.

Figure 9 shows the absorption patterns in the QW stack near the spiral for two different wavelengths of illumination. The pattern oscillates as one moves along the winding, as expected from the previously stated operating mechanism. The physical mechanism behind the antenna's broad spectral bandwidth is also apparent. Note that the absorption pattern rotates around the antenna windings as the wavelength is varied, but maintains nearly the same total absorption.

Figure 8. Calculated spectral QE for antenna-coupled QWIP with 3×3 array of spiral antennas. Conductivity is "synthetic" conductivity corresponding to indicated reflectances. QW absorption strength is constant.

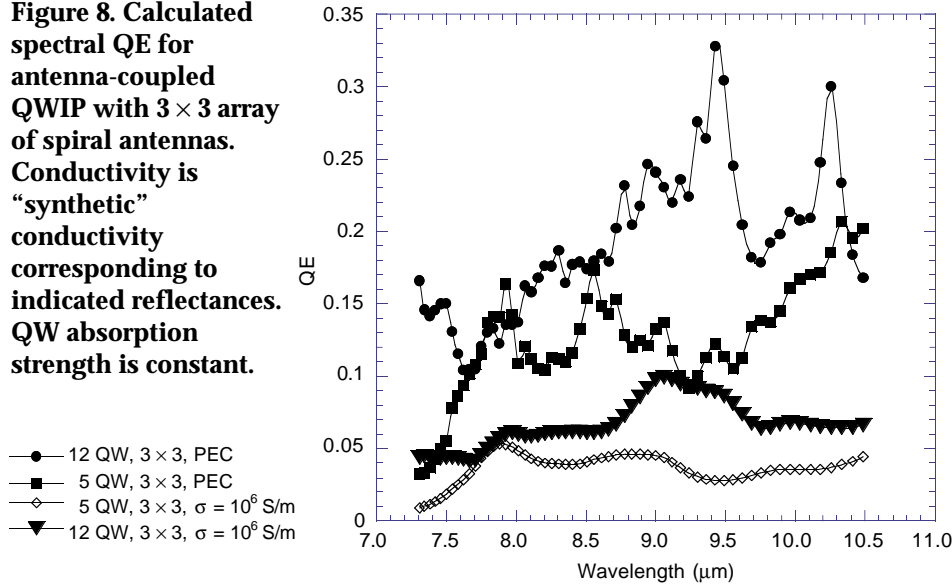
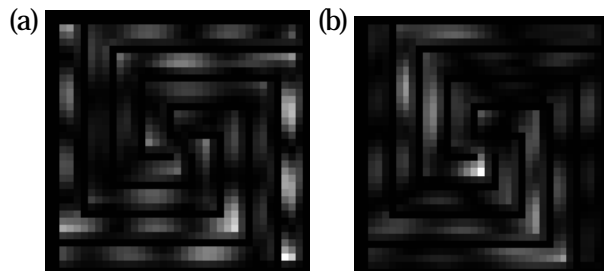


Figure 9. Absorption in QW stack near spiral antennas at (a) 9.42 μm and (b) 9.06 μm . Structure has 12 QWs with PEC antenna.



Jigsaw Antenna

The jigsaw antenna pattern is shown in figure 10. It was originally designed as a set of vertical and horizontal lines that had U-shaped shunts to induce out-of-phase currents in neighboring lines similar to those induced in the spiral antenna, but with a longer decay length away from the antenna plane. The pattern could then couple to thicker QW stacks for applications where maximum QE is the most important criterion.

However, after optimizing the dimensions using the infinite-pixel model, we found that the pattern contains an overall period of $\sim 18\ \mu\text{m}$ and a “sub-period” (of the lines in the pattern) of $\sim 3\ \mu\text{m}$. Therefore, the pattern acts much like a $3\text{-}\mu\text{m}$ period planar metal grating. However, since the pattern has an $18\text{-}\mu\text{m}$ period, it supports approximately 36 ($18/3$, squared) times as many propagating modes as the pure $3\text{-}\mu\text{m}$ period grating. With the proper layer thicknesses, these modes combine to suppress rediffraction out of the detector, thereby yielding high QE.

We modeled a jigsaw antenna-coupled pixel with 40 QWs that contained 2×2 unit cells, 3×3 unit cells, and an infinitely periodic pixel. A cell size of $0.3 \times 0.3 \times 0.3\ \mu\text{m}$ was used with 16,384 time steps. The time step length was equal to the Courant value of $5.65 \times 10^{-16}\ \text{s}$. The results are shown in figure 11. The figure includes results for both PEC and finite-conductivity antennas, but with the previously mentioned warning about the uncertainty of the synthetic conductivity method for a one-cell-thick antenna. Note that the spectral QE is high over a broad spectral range for the infinite pixel. However, the QE of the 3×3 and 2×2 period pixels are progressively degraded due to finite-pixel size effects, consistent with this design’s use of propagating modes.

Figure 10. 2×2 periods of jigsaw antenna in $38\text{-}\mu\text{m}$ pixel. Metal is dark.

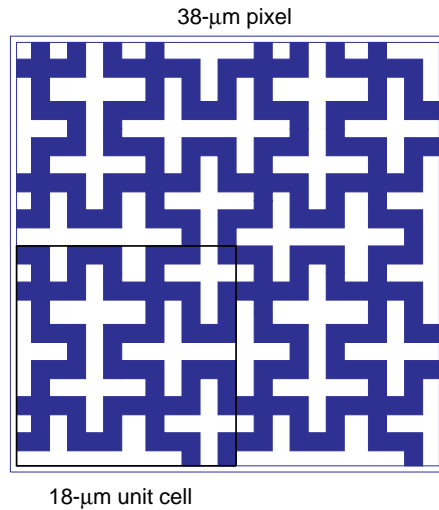
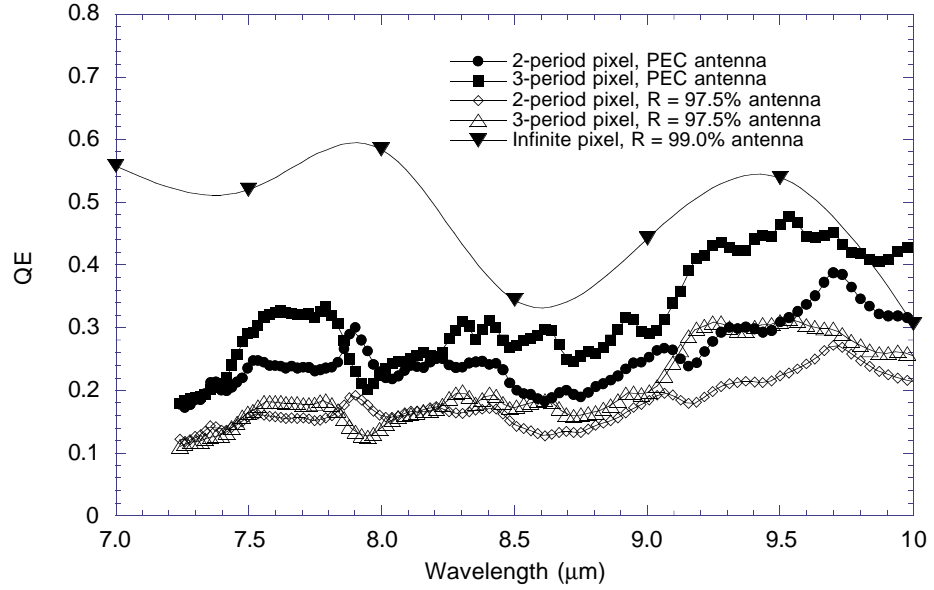


Figure 11. Calculated QE for several pixel sizes using jigsaw antenna coupler. Finite pixels are calculated by FDTD. Infinite pixel is calculated by MEM.



Conclusions

Planar antennas offer several benefits as optical couplers in QWIPs. Use of planar metal layers eliminates the need for a grating etch and the potential nonuniformity associated with that etch. All of the processing except for deposition of the AR coating is done on the front (MBE growth) side of the wafer so there is no need for backside processing of individual die or handling of fully thinned wafers, as with some other approaches.

As demonstrated by the calculated spectral QE for the spiral antenna array, a relatively high QE can be obtained over a wide spectral band, even with a reduced number of QWs. This should permit increased detectivity in dark-current-limited QWIPs at elevated operating temperature.

We have also presented the first numerical modeling of QWIPs using the FDTD method and demonstrated the utility of the technique for predicting QE for finite-sized pixels. The undersampled spectral QE technique is particularly useful, since it yields the full spectral response in a single FDTD run. After more validation of the predicted results with experiment, the technique should be a very useful tool for designing and optimizing realistically sized QWIP pixels.

Acknowledgments

We gratefully acknowledge helpful correspondence with Raymond Luebbers on use of the FDTD method with finite conducting metals. We also thank Dennis Prather for many helpful discussions.

References

1. G. Hasnain, B. F. Levine, C. G. Bethea, R. A. Logan, J. Walker, and R. J. Malik, Appl. Phys. Lett. **54**, 2515 (1989).
2. J. Y. Andersson and L. Lundqvist, Appl. Phys. Lett. **59**, 857 (1991).
3. J. Y. Andersson, L. Lundqvist, and Z. F. Paska, Appl. Phys. Lett. **58**, 2264 (1991).
4. J. Y. Andersson and L. Lundqvist, J. Appl. Phys. **71**, 3600–3610 (1992).
5. J. Y. Andersson and L. Lundqvist, J. Appl. Phys. **71**, 3600 (1992).
6. G. Sarusi, B. F. Levine, S. J. Pearton, K.M.S. Bandara, and R. E. Leibenguth, Appl. Phys. Lett. **64**, 960 (1994).
7. W. J. Li and B. D. McCombe, J. Appl. Phys. **71**, 1038 (1992).
8. S. D. Gunapala, J. K. Liu, M. Sundaram, J. S. Park, C. A. Shott, T. Hoelter, T. L. Lin, S. T. Massie, P. D. Maker, R. E. Muller, and G. Sarusi, Proc. 188th Meeting of the Electrochemical Society, Chicago, IL (1995).
9. T. R. Schimert, S. L. Barnes, A. J. Brouns, F. C. Case, P. Mitra, and L. T. Claiborne, Appl. Phys. Lett. **68**, 2846 (1996).
10. C. J. Chen, K. K. Choi, M. Z. Tidrow, and D. C. Tsui, Appl. Phys. Lett. **68**, 1446 (1996).
11. P. Yeh, *Optical Waves in Layered Media*, John Wiley & Sons, New York (1988).
12. K. S. Kunz and R. J. Luebbers, *The Finite Difference Time Domain Method in Electromagnetics*, CRC Press, Boca Raton, FL (1993).
13. A. Taflove, *Computational Electrodynamics: The Finite-Difference Time-Domain Method*, Artech House, Boston (1995).
14. Remcom, XFDTD 4.0 for X-Windows, Remcom, Inc., www.remcominc.com, State College, PA (1997).
15. K. Chamberlin and L. Gordon, IEEE Trans. Electromagnetic Compatibility **37**, 210 (1995).
16. M. Born and E. Wolf, *Principles of Optics*, Sixth ed., Pergamon Press, New York (1980).
17. CRC, in *CRC Handbook of Chemistry and Physics*, CRC Press, Boca Raton, FL (1988), E-93.
18. R. G. Corzine and J. A. Mosko, *Four-Arm Spiral Antennas*, Artech House, Norwood (1990).

Contents

Introduction	1
Antenna-Coupled QWIP Structure	3
Modeling Techniques	4
<i>Coupled Mode (Infinite Pixel)</i>	4
<i>Finite-Difference Time Domain (Finite Pixel)</i>	5
Results	9
<i>Two-Dimensional, Square-Cavity Grating</i>	9
<i>Spiral Antenna</i>	11
<i>Jigsaw Antenna</i>	13
Conclusions	14
Acknowledgments	14
References	15
Distribution	17
Report Documentation Page	21

Figures

1. Typical grating-coupled QWIP pixel	1
2. Cross section of antenna-coupled pixel	3
3. 3×3 array of four-arm spiral antennas	5
4. Time-dependent electric fields and incident and absorbed power and QE near center of 50- μm pixel	8
5. Cross section of square-grating-coupled structure	9
6. Calculated spectral QE for 39- μm pixel with 3- μm -period, two-dimensional, square-cavity grating	10
7. Operation of spiral antenna	10
8. Calculated spectral QE for antenna-coupled QWIP with 3×3 array of spiral antennas	12
9. Absorption in QW stack near spiral antennas	12
10. 2×2 periods of jigsaw antenna in 38- μm pixel	13
11. Calculated QE for several pixel sizes using jigsaw antenna coupler	14

Table

1. Material properties used in FDTD calculations	7
--	---

Distribution

Admnstr
Defns Techl Info Ctr
Attn DTIC-OCF
8725 John J Kingman Rd Ste 0944
FT Belvoir VA 22060-6218

Ballistic Mis Defns Ofc
Innovative Sci and Technl
Attn D Duston
Attn W Dyer
7100 Defense The Pentagon
Washington DC 20301-7100

Inst for Defns Analyses Sci & Techlgy Div
Attn G Hopper
Attn K Carson
Attn R Singer
1801 N Beauregard Stret
Alexandria VA 22311-1772

Ofc of the Dir Rsrch and Engrg
Attn R Menz
Pentagon Rm 3E1089
Washington DC 20301-3080

Ofc of the Secy of Defns
Attn ODDRE (R&AT) G Singley
Attn ODDRE (R&AT) S Gontarek
The Pentagon
Washington DC 20301-3080

OSD
Attn OUSD(A&T)/ODDDR&E(R) R Tru
Washington DC 20301-7100

Army Rsrch Ofc
Attn AMXRO-GS Bach
Attn H Everitt
PO Box 12211
Research Triangle Park NC 27709

Army Rsrch Ofc
Attn M Strosio
4300 S Miami Blvd
Research Triangle Park NJ 27709

Army Rsrch Physics Div
Attn AMXRO-PH D Skatrud
Research Triangle Park NC 27709

CECOM
Attn PM GPS COL S Young
FT Monmouth NJ 07703

CECOM RDEC Elect System Div Dir
Attn J Niemela
FT Monmouth NJ 07703

CECOM
Sp & Terrestrial Commctn Div
Attn AMSEL-RD-ST-MC-M H Soicher
FT Monmouth NJ 07703-5203

DARPA
Attn R Balcerak
3701 N Fairfax Dr
Arlington VA 22203-1714

Dir for MANPRINT
Ofc of the Deputy Chief of Staff for Prsnl
Attn J Hiller
The Pentagon Rm 2C733
Washington DC 20301-0300

Dpty Assist Secy for Rsrch & Techl
Attn SARD-TT F Milton Rm 3E479
The Pentagon
Washington DC 20301-0103

Hdqtrs Dept of the Army
Attn DAMO-FDT D Schmidt
400 Army Pentagon Rm 3C514
Washington DC 20301-0460

MICOM RDEC
Attn AMSMI-RD W C McCorkle
Redstone Arsenal AL 35898-5240

Night Vision & Elec Sensors Dir
Attn AMSEL-RD-NV-OD J Ratches
Attn AMSEL-RD-NV-OV J Pollard
10221 Burbeck Rd Ste 430
FT Belvoir VA 22060-5806

TECOM
Attn AMSTE-CL
Aberdeen Proving Ground MD 21005-5057

Distribution

US Army CECOM
Rsrch, Dev, & Engrg Ctr
Attn R F Giordano
FT Monmouth NJ 07703-5201

US Army Edgewood
Rsrch, Dev, & Engrg Ctr
Attn SCBRD-TD J Vervier
Aberdeen Proving Ground MD 21010-5423

US Army Info Sys Engrg Cmnd
Attn ASQB-OTD F Jenia
FT Huachuca AZ 85613-5300

US Army Materiel Sys Analysis Agency
Attn AMXSU-D J McCarthy
Aberdeen Proving Ground MD 21005-5071

US Army Matl Cmnd
Dpty CG for RDE Hdqtrs
Attn AMCRD BG Beauchamp
5001 Eisenhower Ave
Alexandria VA 22333-0001

US Army Matl Cmnd
Prin Dpty for Acquisition Hdqtrs
Attn AMCDCG-A D Adams
5001 Eisenhower Ave
Alexandria VA 22333-0001

US Army Matl Cmnd
Prin Dpty for Techlgy Hdqtrs
Attn AMCDCG-T M Fisette
5001 Eisenhower Ave
Alexandria VA 22333-0001

US Army Natick Rsrch, Dev, & Engrg Ctr
Acting Techl Dir
Attn SSCNC-T P Brandler
Natick MA 01760-5002

US Army Rsrch Ofc
Attn G Iafrate
4300 S Miami Blvd
Research Triangle Park NC 27709

US Army Simulation, Train, & Instrmntn
Cmnd
Attn J Stahl
12350 Research Parkway
Orlando FL 32826-3726

US Army Tank-Automtv & Armaments Cmnd
Attn AMSTA-AR-TD C Spinelli
Bldg 1
Picatinny Arsenal NJ 07806-5000

US Army Tank-Automtv Cmnd
Rsrch, Dev, & Engrg Ctr
Attn AMSTA-TA J Chapin
Warren MI 48397-5000

US Army Test & Eval Cmnd
Attn R G Pollard III
Aberdeen Proving Ground MD 21005-5055

US Army Train & Doctrine Cmnd
Battle Lab Integration & Techl Dirctr
Attn ATCD-B J A Klevecz
FT Monroe VA 23651-5850

US Military Academy
Dept of Mathematical Sci
Attn MAJ D Engen
West Point NY 10996

USAASA
Attn MOAS-AI W Parron
9325 Gunston Rd Ste N319
FT Belvoir VA 22060-5582

Nav Rsrch Lab
Attn Code 6818 J Omaggio
Washington DC 20375

Nav Rsrch Lab
Attn Code 5636 M Kruer
4555 Overlook Ave
Washington DC 20375-5000

Nav Surface Warfare Ctr
Attn Code B07 J Pennella
17320 Dahlgren Rd Bldg 1470 Rm 1101
Dahlgren VA 22448-5100

NVESD
Attn AMSEL-RD-NV-ST-IRT S Horn
10221 Burbeck Rd
FT Belvoir VA 22060-5806

AFOSR/NE
Attn M Prarie
110 Duncan Ave Ste B115
Bolling AFB DC 20332-6448

Distribution

GPS Joint Prog Ofc Dir
Attn COL J Clay
2435 Vela Way Ste 1613
Los Angeles AFB CA 90245-5500

US Air Force Phillips Lab
Attn PL/VTE R Pugh
3550 Aberdeen Ave SE
Kirtland AFB NM 87117

DARPA
Attn B Kaspar
Attn L Stotts
3701 N Fairfax Dr
Arlington VA 22203-1714

NASA Goddard Solid State Device Dev Br
Attn Code 718 M Jhabvala
Bldg 11 Rm E23
Greenbelt MD 20771

ARL Electromag Group
Attn Campus Mail Code F0250 A Tucker
University of Texas
Austin TX 78712

Virginia Tech Dept of Materials Sci & Engrg
Attn S Desu
213 Holden Hall
Blacksburg VA 24061

Hughes Rsrch Lab
Attn J Jensen
3011 Malibu Rd
Malibu CA 90265

Lockheed Martin Sanders
Attn MS NHQ 6-1517 J Ahearn
65 Split Brooke Rd
Nashua NH 03061-0868

Palisades Inst for Rsrch Svc Inc
Attn E Carr
1745 Jefferson Davis Hwy Ste 500
Arlington VA 22202-3402

Ratheon TI Systems
Attn C Hanson
13532 N Central Expwy MS 37
Dallas TX 75265

Raytheon TI Systems
Attn H F Schaaake
PO Box 655936 MS 150
Dallas Tx 75265

Rockwell Internatl Sci Ctr Elect Dev Lab
Attn B Tennant
1049 Camino Dos Rios
Thousand Oaks CA 91360

SRI Internatl
Attn A Sher
333 Ravenswood Ave
Menlo Park CA 94025

US Army Rsrch Lab
Attn J Zavada
PO Box 12211
Research Triangle Park NC 27709-2211

US Army Rsrch lab
Attn AMSRL-CI-LL Techl Lib (3 copies)
Attn AMSRL-CS-AL-TA Mail & Records
Mgmt
Attn AMSRL-CS-AL-TP Techl Pub (3 copies)
Attn AMSRL-MA-G S Sengupta
Attn AMSRL-SE-EE B Beck (20 copies)
Adelphi MD 20783-1197

REPORT DOCUMENTATION PAGE			Form Approved OMB No. 0704-0188	
Public reporting burden for this collection of information is estimated to average 1 hour per response, including the time for reviewing instructions, searching existing data sources, gathering and maintaining the data needed, and completing and reviewing the collection of information. Send comments regarding this burden estimate or any other aspect of this collection of information, including suggestions for reducing this burden, to Washington Headquarters Services, Directorate for Information Operations and Reports, 1215 Jefferson Davis Highway, Suite 1204, Arlington, VA 22202-4302, and to the Office of Management and Budget, Paperwork Reduction Project (0704-0188), Washington, DC 20503.				
1. AGENCY USE ONLY (Leave blank)		2. REPORT DATE March 1998		3. REPORT TYPE AND DATES COVERED Final, from Oct 1996 to July 1997
4. TITLE AND SUBTITLE Antenna Structures for Optical Coupling in Quantum-Well Infrared Detectors			5. FUNDING NUMBERS PE: 61102A	
6. AUTHOR(S) William A. Beck (ARL), Mark S. Mirotznik (Catholic U), and Thomas S. Faska (Sanders)				
7. PERFORMING ORGANIZATION NAME(S) AND ADDRESS(ES) U.S. Army Research Laboratory Attn: AMSRL-SE-EE (wbeck@arl.mil) 2800 Powder Mill Road Adelphi, MD 20783-1197			8. PERFORMING ORGANIZATION REPORT NUMBER ARL-TR-1533	
9. SPONSORING/MONITORING AGENCY NAME(S) AND ADDRESS(ES) U.S. Army Research Laboratory 2800 Powder Mill Road Adelphi, MD 20783-1197			10. SPONSORING/MONITORING AGENCY REPORT NUMBER	
11. SUPPLEMENTARY NOTES AMS code: 611102.H44 ARL PR: 7NE3GG				
12a. DISTRIBUTION/AVAILABILITY STATEMENT Approved for public release; distribution unlimited.			12b. DISTRIBUTION CODE	
13. ABSTRACT (Maximum 200 words) Predicted performance for antenna-coupled, quantum-well infrared photodetectors (QWIPs) is presented. These structures contain a patterned metal antenna layer and dielectric backplane reflector in place of the usual metal phase grating. When illuminated by normally incident plane-wave illumination, the antenna structures generate both evanescent and propagating modes that have the required polarization to be absorbed by the QW stack. An undersampled spectral technique is also demonstrated for using the finite-difference, time-domain (FDTD) technique to compute spectral quantum efficiency in a single FDTD run.				
14. SUBJECT TERMS Quantum well, infrared detector, antenna			15. NUMBER OF PAGES 25	
			16. PRICE CODE	
17. SECURITY CLASSIFICATION OF REPORT Unclassified	18. SECURITY CLASSIFICATION OF THIS PAGE Unclassified	19. SECURITY CLASSIFICATION OF ABSTRACT Unclassified	20. LIMITATION OF ABSTRACT UL	

DEPARTMENT OF THE ARMY
U.S. Army Research Laboratory
2800 Powder Mill Road
Adelphi, MD 20783-1197

An Equal Opportunity Employer